Contents lists available at ScienceDirect

Applied Catalysis B: Environmental

Nanobelt-arrayed vanadium oxide hierarchical microspheres as catalysts for selective oxidation of 5-hydroxymethylfurfural toward 2,5-diformylfuran

Yibo Yan, Kaixin Li, Jun Zhao, Weizheng Cai, Yanhui Yang*, Jong-Min Lee*

School of Chemical and Biomedical Engineering, Nanyang Technological University, Singapore 637459, Singapore

ABSTRACT

Nanobelt-arrayed vanadium oxide hierarchical microspheres were synthesized to catalyze selective oxidation of 5-hydroxymethylfurfural to 2,5-diformylfuran with the high conversion and selectivity of 93.7% and 95.4%, respectively. This prominent performance can be attributed to the major exposure of (010) facet with highest hydrogen adsorption capability of vanadyl group (V═O) sites and the highly oriented morphology for reactant contact and residence time control. Density functional theory calculation of the hydrogen adsorption capabilities on different facets and different chemical environmental sites has been utilized to explain the influence of different facets and lattice oxygen sites on 5-hydroxymethylfurfural oxidation performance based on hydrogen adsorption and αH-C bond cleavage steps. Isotopic studies verified the reaction mechanism and kinetic studies derived the first order reaction rate equation dependent on the 5-hydroxymethylfurfural concentration. These results suggested the crucial roles of (0 1 0) facets and the V═O sites in O-H and αH-C bonds cleavage of 5-hydroxymethylfurfural before the reduction product V-OH species further dehydrogenation by molecular oxygen.

© 2017 Elsevier B.V. All rights reserved.

1. Introduction

Biomass as a widely reproducible energy source derived from CO_2 fixation is drawing more attention as the alternative to limited fossil fuels. Biomass conversion into fuels and high value-add chemicals, also known as biorefinery process, occupied much effort and various methods [1–3]. 5-Hydroxymethylfurfural (HMF) generated from C6-carbonhydrates dehydration, has been expected as a crucial precursor for valuable chemicals such as 2,5-diformylfuran (DFF), 5-hydroxymethyl-2-furancarboxylic acid (HMFCA), and 2,5-furandicarboxylic acid (FDCA), among which DFF renders a most versatile intermediate transforming to numerous furan-containing functional polymers, pharmaceuticals, poly-Schiff bases, organic conductors and antifungal agents [2].

HMF oxidation to DFF encounters some challenge due to the reactive α,β-unsaturated aldehyde group on HMF. To date, selective oxidation of HMF to DFF has employed plenty of catalysts such as the manganese oxide octahedral molecular sieve [4], graphene oxide with 2,2,6,6-tetramethylpiperidin-1-oxyl (TEMPO) [2], ruthenium supported on Mg–Al hydrotalcite [5],

and vanadium-based catalysts [6–8]. Among them, vanadium-containing catalysts are noticeable owing to the high selectivity toward DFF (> 90%) at low cost with unclear reaction mechanism simply comprised of the iterative redox cycles of V^{5+} oxidizing HMF and V^{4+} oxidized by O_2 [9]. Conventional VO_x-based catalysts are usually associated with the vanadium-heteropolyacid [1], bulk VO_x, and supported VO_x [10]. The structure of VO_x varies from monovanadate and polyvanadate with crystal structure depending on valence condition. Nevertheless, the detailed mechanism exploration and kinetic studies involving VO_x physical morphology, crystalline structure and types of active sites were hardly found.

Here, we intend to synthesize a hierarchical structure of vanadium oxide nanobelt-arrayed mesoporous microsphere (VO_x-ms) for detailed investigation of the influence of morphology, crystalline facet, valence condition, hydrogen adsorption capabilities and adsorption convenience on catalytic performance in the selective oxidation of HMF to DFF. Structures, hydrogen adsorption capabilities on different active sites and active sites distribution are illuminated by field emission scanning electron microscopy (FESEM), transmission electron microscopy (TEM), high-resolution transmission electron microscopy (HRTEM), X-ray diffraction (XRD), X-ray photoelectron spectroscopy (XPS), Brunauer–Emmett–Teller (BET) and density functional theory (DFT) calculations.

* Corresponding authors.
E-mail addresses: yhyang@ntu.edu.sg (Y. Yang), jmlee@ntu.edu.sg (J.-M. Lee).

2. Experimental

2.1. Material preparation

The VO_x-ms utilized in this study were synthesized by solvothermal process before calcination. 0.5 mL of vanadium oxytriethoxide [$VO(OC_2H_5)_3$] was mixed with 15 mL of acetic acid in a Teflon-lined autoclave (45 mL) followed by stirring for 10 min. This sealed autoclave was located in a 200 °C oven for 1.5 h. After cooling down to room temperature, the product was centrifugated and washed several times with ethanol, then dried at 80 °C overnight. Subsequently, the VO_x-ms was achieved after calcination at 350 °C for 10 min (heating rate 0.5 °C min^{-1}) under air.

2.2. Characterizations

X-ray powder diffraction (XRD, GBC MMA diffractometer, Cu Kα radiation, wave length 0.15406 nm) was performed to characterize the crystalline structures. Filed-emission scanning electron microscopy (FESEM JEOL JSM-6701) was utilized to observe the morphology of materials. Transmission electron microscopy observations were conducted on a JEOL JEM 2010 200 kV TEM instrument. The specific surface area calculated by BET method was examined by the adsorption isotherms of nitrogen at −196 °C with Quantachrome Aurosorb-6B apparatus. ESCALAB 250XI photoelectron spectrometer (Thermo Fisher Scientific, USA) spectrometer and the Al Kα 1846.6 eV anode were employed to measure the XPS spectra, with C 1s peak at 284.6 eV as the reference for binding energy calibration.

2.3. Computational methods and models

The structure optimization and overall energy calculations were acquired by DFT code DMol^3 within Material Studio package of Accelerys [11]. Local density approximation together with the generalized gradient correction (GGA-PW91) was employed for the exchange-correlation functional method [12–14]. Double numerical basis set with all atoms in polarization function (DNP basis set) was performed. Vacuum thickness at 10 Å was set for periodic system to eradicate spurious interactions between adsorbate and periodic bottom-layer surface image [15]. 4.4 Å of real space cut-off was set to enhance computational performance. Self-consistent field computation set the energy tolerance as 1.0×10^{-5} E_h. Energy convergence tolerance (2.0×10^{-5} E_h) and gradient convergence (5×10^{-5} E_h/A) were utilized for geometry optimization. The adsorption energy E_{ads} was calculated based on: $E_{ads} = E_{(adsorbate/substrate)} - E_{adsorbate} - E_{substrate}$, where $E_{(adsorbate/substrate)}$ denoted the overall energy of

adsorbate/substrate, $E_{adsorbate}$ represented merely adsorbate, and $E_{substrate}$ represented merely the substrate. More negative E_{ads} indicates more stable system of adsorbate/substrate after adsorption.

2.4. Catalytic performance in selective oxidation of HMF

HMF oxidation reactions were performed in a Teflon-lined (25 mL) Parr high pressure reactor (Parr Instrument, USA). Typically, 1.0 mmol HMF dissolved in 10 mL ultrapure water was applied with 100 mg of catalysts, stirred at 800 rpm. The liquid phase was analyzed by high performance liquid

chromatography (HPLC, Agilent 1260 Infinity) armed with UV detector (VWD, G1314B, 1260 VWD VL), refractive index detector (RID, G1362A 1260), thermostatted column compartment (TCC, G1316A), G1322A standard degasser and Bio-Rad Aminex HPX-87H, 300 mm × 7.8 mm pre-packed column using 5 mM H_2SO_4 as mobile phase.
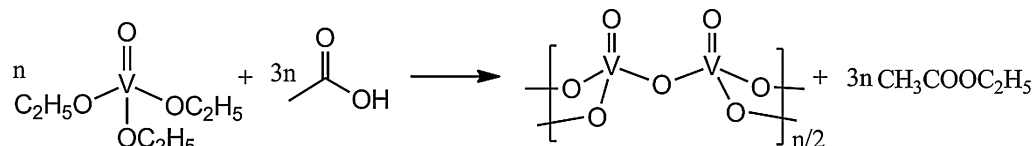
2.5. Kinetic isotope and oxygen isotope studies

Kinetic isotope examination was carried out using deuterated HMF, including α-deuterated HMF (CHO-C_4H_2O-CH_2OD, simplified as RCH_2OD) and β-deuterated HMF (CHO-C_4H_2O-CD_2OH, simplified as RCD_2OH), as the benchmark of ordinary HMF oxidation. Oxygen isotope exchange was examined using $^{18}O_2$ to compare with $^{16}O_2$, for oxygen exchange process detection during HMF oxidation reaction.

3. Results and discussion

3.1. Characterization of VO_x-ms catalyst

FESEM observations displayed in Fig. 1a, b, c represented the solvothermal generation process of VO_x-ms precursor at 15 min, 30 min and 1.5 h respectively. The magnification image of single VO_x microsphere after calcination is exhibited in Fig. 1d, with nanobelts orderly arrayed to assemble the sphere. The TEM observation in Fig. 1e verified the orderly arrayed nanobelts to form the VO_x microspheres, with the lattice space of 0.41 nm characterized by HRTEM. The XRD pattern in Fig. 2a illustrated the typical V_2O_5 crystal structure with JCPDS card 41-1426 for both the commercial bulk V_2O_5 powder and the VO_x-ms. However, the VO_x-ms demonstrated the largely enhanced (0 1 0) facet signal ($2\theta = 21.7°$) than other facet signals of VO_x-ms, implying the majority exposure of the (0 1 0) facet. Coincidently, the (0 1 0) facet signal at 21.7° corresponded to the 0.41 nm of facet spacing according to the Bragg's Law, further verifying the HRTEM result. For characterization of the valence state of vanadium in VO_x-ms, XPS was performed as shown in Fig. 2b with the inset involving the V $2p_{1/2}$ and V $2p_{3/2}$ binding energy at 525 eV and 517 eV, respectively. The O 1s binding energy at 530 eV identified the O^{2-} ions. Such XPS spectra are typically in accordance with the V_2O_5 XPS spectra [16]. Both the XRD and XPS spectra illuminated that V_2O_5 made the major component of VO_x-ms.

The growth process for this nanobelt-assembled microsphere is illustrated by Fig. 3. First, during the nucleation and aggregation step, the reaction between vanadium oxytriethoxide and acetic acid removed the –OC_2H_5 and formed V-O-V bond through ligand substitution:

$$n \quad \underset{\underset{OC_2H_5}{C_2H_5O}}{\overset{\overset{O}{\parallel}}{V}} \hspace{-0.3em}-\hspace{-0.3em} OC_2H_5 \; + \; 3n \; \overset{O}{\underset{OH}{\parallel}} \quad \longrightarrow \quad \left[\underset{O}{\overset{O}{\underset{|}{\overset{\parallel}{V}}}} \hspace{-0.3em} O \hspace{-0.3em} \underset{O}{\overset{O}{\underset{|}{\overset{\parallel}{V}}}} \hspace{-0.3em} O \right]_{n/2} \; + \; 3n \; CH_3COOC_2H_5$$

Plenty of nucleus were generated rapidly and subsequently precipitated into nanobelt-shaped nanocrystals (intermediate product solvothermally reacted for 15 min) as displayed by Fig. 1a. Second, for the surface energy minimization, these nanobelts self-assembled and orderly arrayed to form the bundles of precursor (intermediate product solvothermally reacted for 30 min) as shown in Fig. 1b. Consequently, long reaction time shaped the microsphere outline of these nanobelt-arrayed bundles, as is indicated by Fig. 1c of the product solvothermally reacted for 1.5 h. After calcination with slow heating rate, the final product VO_x-ms retained the morphology of the nanobelt-arrayed hierarchical microspheres. The
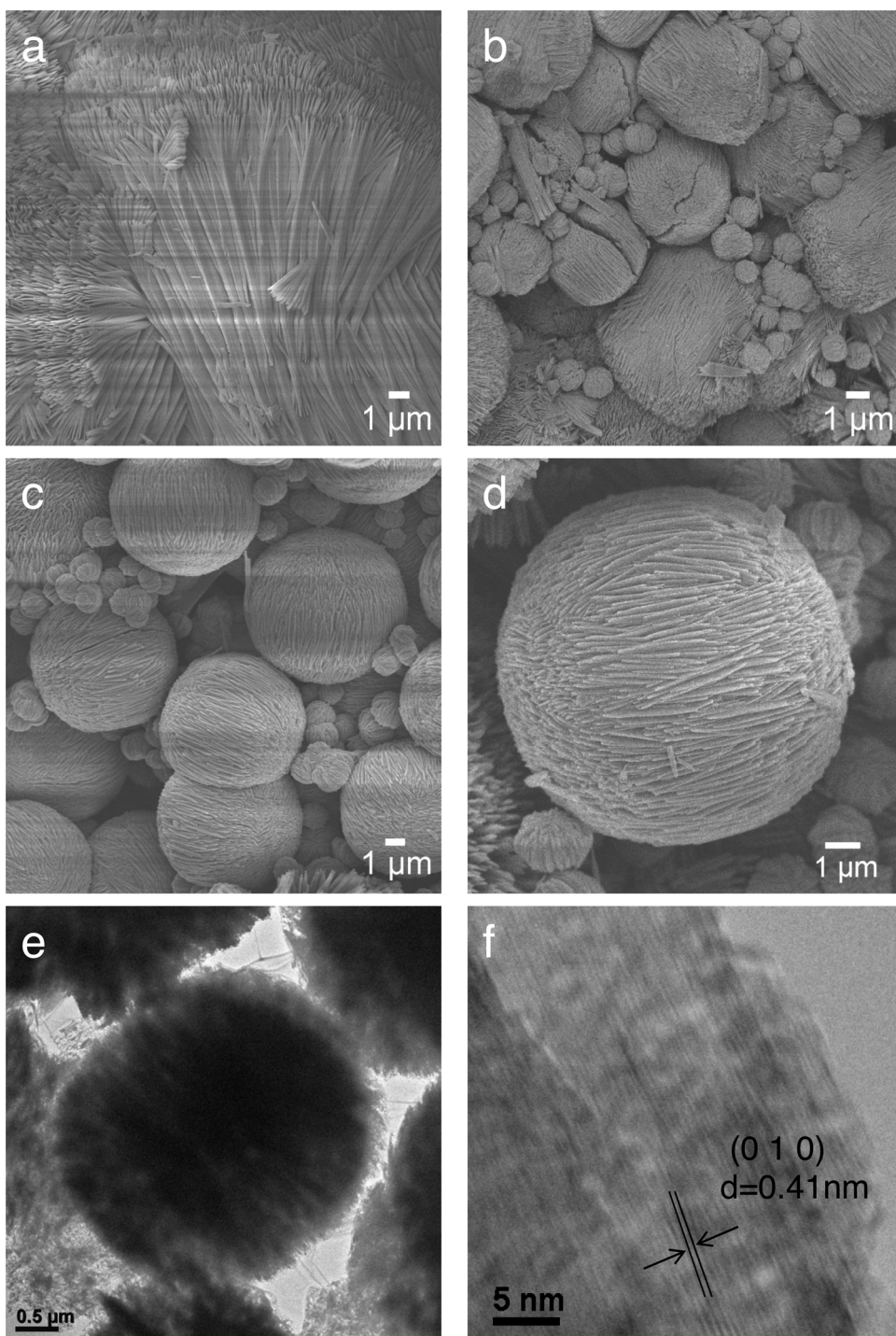
Fig. 1. (A) FESEM image of VO_x-ms synthesized at 200 °C for 15 min. (B) FESEM image of VO_x-ms synthesized for 30 min. (C) FESEM image of VO_x-ms synthesized for 1.5 h. (D) High magnification FESEM image of single VO_x-ms after calcination. (E) TEM image VO_x-ms. (F) HRTEM of nanoparticles forming the nanobelts of VO_x-ms.

nitrogen adsorption-desorption isotherms were monitored with BET analysis exhibited in Fig. 4, and the specific surface area of VO_x-ms was measured to be 117.2 m² g⁻¹ with typical H3-type hysteresis mesoporous pattern [17–19].

3.2. DFT computation of hydrogen adsorption capabilities

For further investigation of the hydrogen adsorption capabilities on different low-index facets, density functional theory (DFT) calculation was utilized. The V_2O_5 crystal possesses the unit cell

parameters with $a = 11.51$ Å, $b = 3.56$ Å, $c = 4.37$ Å [20]. Optimization of these parameters generated $c = 4.42$ Å instead besides the same a, b values. It has three low-index facets of (0 0 1), (0 1 0) and (1 0 0). On (0 0 1) plane, there are three sorts of oxygen including the O(1) at V=O sites, O(2) with double coordination, and O(3) with triple coordination, as displayed in Fig. 5. On the (0 1 0) facet, there are concave-convex regions. Accordingly, three sorts of lattice oxygen involving the single coordinated O(1) on vanadyl bond, the bridging O(2) with double coordination connecting two adjacent V atoms, and a new O(3) at the edge of "hill"
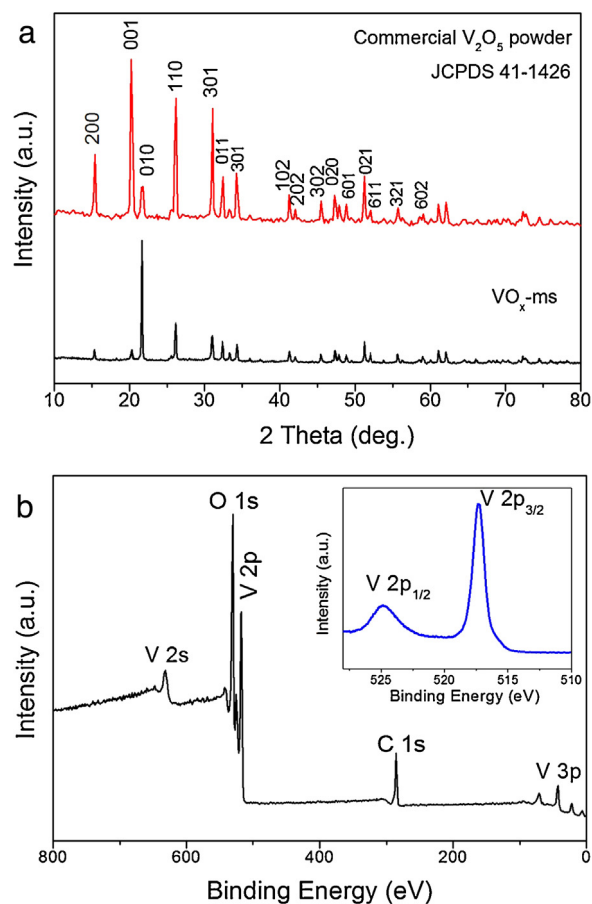
Fig. 2. (A) XRD patterns of VO_x-ms and commercial VO_x powder. (B) XPS spectra of VO_x-ms.
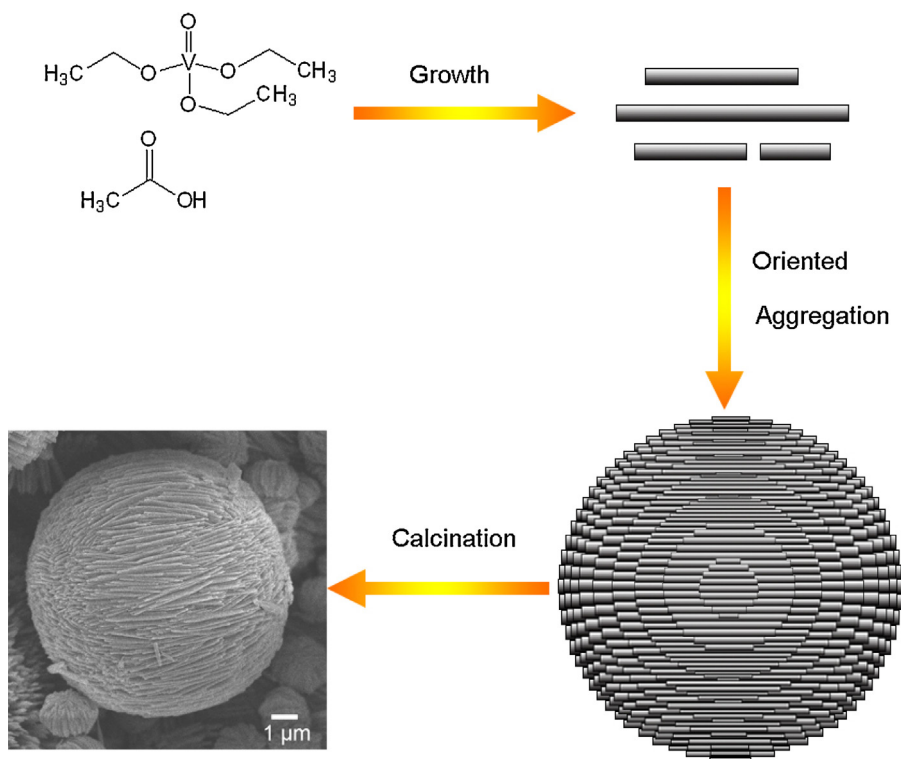

Fig. 3. Schematic diagram of the nanobelt-arrayed growth process of VO_x-ms.

Table 1
Hydrogen adsorption energies of hydrogen atom E_{ads}^{H} and hydrogen molecules E_{ads}^{H} (0.5H$_2$) at different oxygen sites on (0 0 1), (0 1 0) and (1 0 0) facets, bond length of O-H d(O-H) derived by hydrogen adsorption and the hydrogen bond length d(OH...O).

|	V$_2$O$_5$ (0 0 1)			V$_2$O$_5$ (0 1 0)			V$_2$O$_5$ (1 0 0)	
	O(1)	O(2)	O(3)	O(1)	O(2)	O(3)	O(1)	O(2)
E_{ads}^{H} (kcal/mol)	−73.6	−74.1	−71.6	−114.2	−112.2	−111.6	−109.3	−91.5
E_{ads}^{H} (0.5H$_2$) (kcal/mol)	−23.3	−23.8	−21.3	−63.9	−61.9	−61.3	−59.0	−41.2
d(H-O) (Å)	0.989	0.977	0.978	1.008	1.048	0.978	1.001	0.986
d(OH...O) (Å)	2.118	–	–	1.667	1.450	–	1.698	2.017
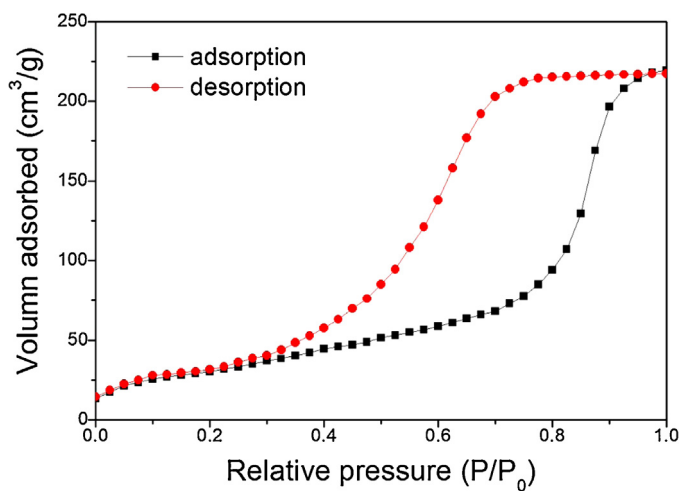
Fig. 4. Nitrogen adsorption–desorption isotherms for BET measurements of VO$_x$-ms.

part derived from triple-coordinated oxygen in bulk. On (1 0 0) facet, there are only the single-coordinated O(1) and the bridging double-coordinated O(2). As shown in Fig. 5, the hydrogen adsorption energies, O-H bond and H...O bond lengths for hydrogen adsorption process at different oxygen sites on different facets are listed in Table 1, with full relaxation assumed in the computation. The facet (0 1 0) possesses the hydrogen adsorption capability ranged in the order of O(1) > O(2) > O(3), with the hydrogen adsorption energies at −114.2, −112.2 and −111.6 kcal/mol respectively, much stronger than facet (1 0 0) and (0 0 1). The strongest hydrogen adsorption capability of O(1) can be ascribed to the vanadyl group (V=O). Single-coordinated O(1) is more nucleophilic than the double-coordinated O(2) bridging with two V atoms. The hydrogen adsorption energies E_{ads}^{H} (0.5H$_2$) are 50.3 kcal/mol smaller than E_{ads}^{H} because generating single hydrogen atom before adsorption

consumes 50.3 kcal/mol energy. For (0 0 1) facet, the as-formed O-H bonds upon hydrogen adsorption possess almost the same length. The hydrogen adsorption energies are also close for three sorts of oxygen sites. Regarding the comparison between (0 1 0) and (0 0 1) facets, the O(1) possessed H...O bond lengths of 1.667 and 2.118 Å respectively. The far decreased H...O bond length on O(1) of (0 1 0) corresponding to highly increased hydrogen adsorption energy suggests the important role of hydrogen bond for hydrogen adsorption process. In contrast, the (1 0 0) plane has more flat structure that distorts oxygen sites especially the O(1). Vanadyl groups are not parallel to (1 0 0) plane. Here, hydrogen adsorption energy of O(1) is still larger than O(2), indicating the significance of vanadyl bond. However, the hydrogen bond length of 1.698 Å of O(1) is close to the 1.667 Å of O(1) on (0 1 0) facet. And the hydrogen adsorption energy is only 4.9 kcal/mol lower than the O(1) on (0 1 0) facet, further verifying the importance of hydrogen bond. Therefore, facet (0 1 0) has the strongest capability for hydrogen adsorption among these facets and the O(1) sites possess higher hydrogen adsorption ability than either O(2) or O(3) on (0 1 0) facet, contributed by the vanadyl bond and hydrogen bond.

3.3. HMF oxidation performance

Table 2 demonstrates HMF oxidation to form DFF in water at 130 °C and 3 MPa O$_2$ by Parr high pressure reactor with different catalysts. Since water is the most environmental-friendly polar solvent, it is chosen as the solvent for HMF oxidation reaction. HMF conversion for 1 h reached 93.7% with selectivity of 95.4% toward DFF on VO$_x$-ms catalyst. The selectivity toward 5-formyl-2-furancarboxylic acid (FFCA) and 2,5-furandicarboxylic acid (FDCA) are only 3.2% and 1.4%, respectively, implying the stability of DFF on VO$_x$-ms under the reaction condition we use. For comparison, commercial V$_2$O$_5$ powder presented the relatively lower HMF conversion (82.5%) because of the lower specific surface area related smaller effective surface area. In addition, the high exposure ratio of (0 1 0) facet and the strong hydrogen adsorption capability on V=O
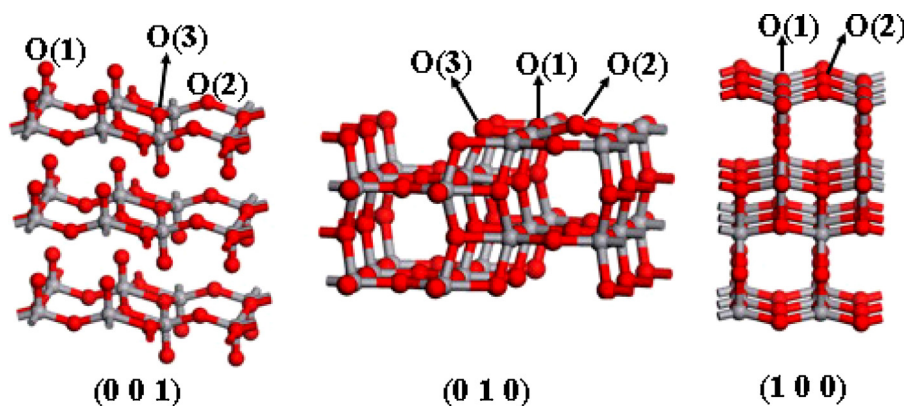
Fig. 5. Three basic low-index V$_2$O$_5$ facets with full relaxation (red balls represent O atom and gray balls represent V atom): DFT calculation for hydrogen adsorption energies at different sites.

Table 2
HMF conversions and products selectivities in high-pressure aerobic oxidation of HMF on different vanadium catalysts and other conventional catalyst for comparison.[a]

Catalyst	Conversion (%)	Selectivity (%)		
		DFF	FFCA	FDCA
VO_x-ms	93.7	95.4	3.2	1.4
V_2O_5 [b]	82.5	94.6	4.8	0.6
VO_2 [b]	74.9	90.3	7.6	2.1
V_2O_3 [b]	62.3	92.7	6.4	0.9
$KMnO_4$ [b]	90.4	41.2	37.7	21.1
$MnSO_4$ [b]	18.5	39.3	34.9	25.8
MnO_2 [b]	56.1	82.7	11.6	5.7
Mn_2O_3 [b]	32.8	69.4	23.5	7.1
Mn_3O_4 [b]	11.2	72.5	18.9	8.6
CrO_3 [b]	75.3	59.6	28.2	12.2
Blank	No reaction	–	–	–

[a] 1.0 mmol HMF, 10 mL H_2O, 100 mg catalyst, 130 °C, 3.0 MPa O_2, 1 h.
[b] Commercial samples powder.

of VO_x-ms (0 1 0) facet contributed to the cleavage of O-H and αH-C bonds on HMF to form DFF. The nanobelt-arrayed microstructure for residence time control may also be crucial for HMF oxidation reaction, compared with bulk V_2O_5 powder. Lower valence of V in VO_2 and V_2O_3 oriented lower activity for HMF oxidation with conversion of 74.9% and 62.3% respectively, suggesting the importance of high valence state of vanadium for HMF oxidation. $KMnO_4$ was also active for HMF oxidation with conversion of 90.4%, yet with the low selectivity toward DFF of only 41.2%, since further oxidation to form FFCA (37.7%) and FDCA (21.1%) easily occurred. Low valence of Mn^{2+} possessed dramatically decreased activity with the evidently low HMF conversion of 18.5%. The catalytic performance of MnO_2, Mn_2O_3 and Mn_3O_4 were also unsatisfactory, with HMF conversion being 56.1%, 32.8% and 11.2%. Low valence state of manganese compounds lead to poor conversion efficiency for HMF oxidation, while high valence state of manganese compound can lead to high activity for HMF oxidation, but with low selectivity toward DFF because over-oxidation to FFCA and FDCA easily happened. CrO_3 was applicable for HMF oxidation as well, but with moderate conversion of 75.3% and selectivity of 59.6%. Accordingly, it can draw a conclusion that VO_x-ms catalyst exhibited the most promising performance for HMF oxidation to DFF among these catalysts due to the high exposure degree of (0 1 0) facet, strong hydrogen adsorption capability and steric advantage of V=O sites on (0 1 0) facet, high effective surface area, specific nanobelt-arrayed morphology for residence time control and the appropriate valence. Furthermore, the convenience of hydrogen bond formation between the lattice oxygen and the O-H group of HMF also facilitates the high selectivity for contact and oxidation of –CH_2OH instead of the –CHO group on HMF, giving rise to high selectivity toward DFF.

Fig. 6 displays the influence of HMF concentrations on catalytic performance involving the conversion and selectivity toward DFF, FFCA and DFCA over VO_x-ms at 130 °C and 3 MPa O_2. The activity values (defined by mmol of reactant converted by per gram of catalyst per hour) almost linearly increased with HMF concentration increased from 10 to 100 mmol/L, and then gradually attained plateau when HMF concentration got 150 mmol/L. The saturation of HMF adsorption on catalyst surface partially determined the catalytic activity. Such phenomena were also observed with many catalysts such as cryptomelane-type manganese oxide molecular sieve (OMS-2) [4], the Ru/C [21] and Ru/Al_2O_3 [22] catalysts. When HMF concentration was low, the reaction rate was expected to be around first order reaction since it was proportional to HMF concentration, when reaction time is held for 1 h. The DFF selectivity mildly decreased from 99.1% to 93.2% with the HMF concentration increasing from 10 to 150 mmol/L.
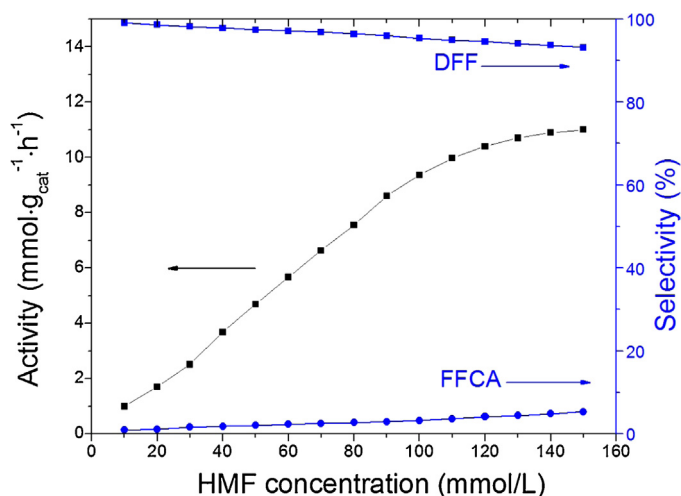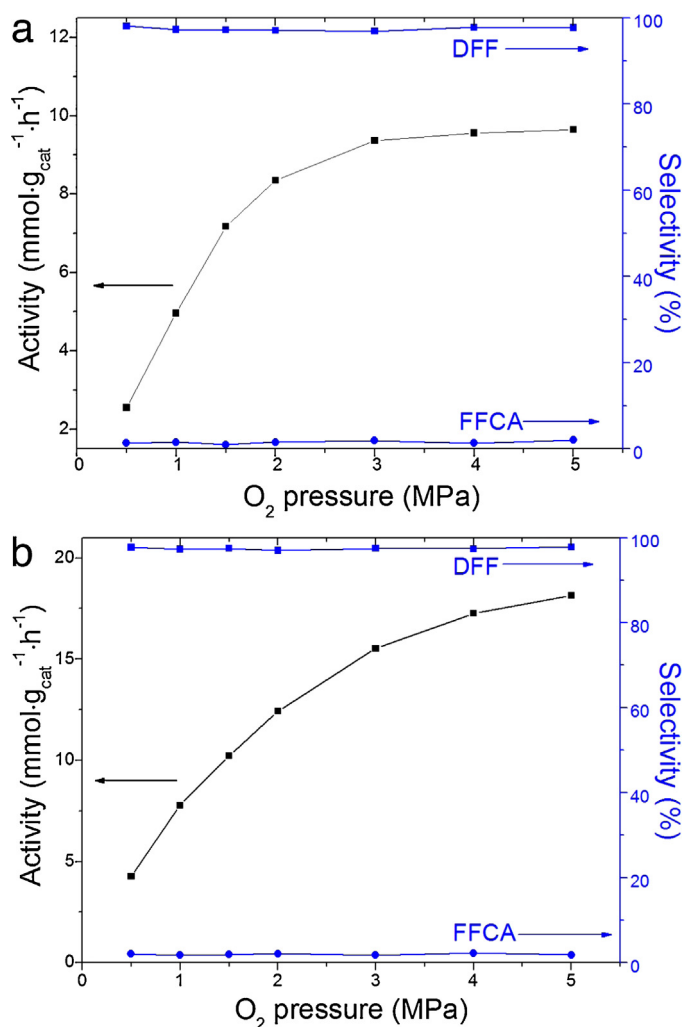

Fig. 6. Reaction activities and selectivities toward DFF and FFCA changed with HMF concentrations in HMF oxidation with high-pressure oxygen. (130 °C, 3 MPa O_2, 0.1–1.5 mmol HMF, 10 mL H_2O, 100 mg VO_x-ms, 1 h).

The influence of oxygen pressure was also investigated for HMF oxidation catalyzed by VO_x-ms. As shown in Fig. 7, selectivity toward DFF and FFCA kept stable, when oxygen pressure increased from 0.5 to 5.0 MPa. Nevertheless, the influence of oxygen pressure on activities varied with high or low concentration of reactant. For a low concentration of HMF (Fig. 7a), the reaction activity first almost linearly increased with O_2 pressure increased from 0.5 to 1.5 MPa and then gradually reached plateau when O_2 pressure got higher than 3 MPa. When O_2 pressure is high enough for low HMF concentration, the influence of O_2 pressure on reaction activity can be neglected. On the other hand, for a high concentration of HMF (Fig. 7b), the reaction activity first almost linearly increased with O_2 pressure increase from 0.5 to 2 MPa and more slowly increased when O_2 pressure got higher than 3 MPa. Saturation of catalytic active surfaces by coverage of reactant, intermediates and products hampered the contact with O_2 and subsequently required higher O_2 pressure to optimize the surface O_2 coverage and reaction activities. The importance of O_2 coverage on surface of vanadium oxide catalysts has been mentioned by Nie et al. that the mechanism involved the V^{5+}/V^{4+} redox cycles and the V^{4+} re-oxidized by molecular O_2 in HMF oxidation to DFF [9].

The effect of temperature and reaction time on reaction activities and selectivities toward DFF and FFCA have been studied and recorded in Fig. 8. The HMF concentration was recorded every 10 min and these HMF concentration-time curves were recorded for reaction temperature at 120, 130 and 140 °C, utilized to fit for reaction rate equation. After mathematical modeling, the reaction rate equations at three temperatures are: $[HMF] = [HMF]_0 \times e^{-0.000462t}$ ($T = 120 °C$), $[HMF] = [HMF]_0 \times e^{-0.000768t}$ ($T = 130 °C$), $[HMF] = [HMF]_0 \times e^{-0.00125t}$ ($T = 140 °C$). These first order decay function type of rate equations illustrate this HMF oxidation catalyzed by VO_x-ms is first order reaction dependent upon HMF concentration under certain reaction conditions and the reaction rate constants are 0.000462, 0.000768 and 0.00125 s^{-1} for 120, 130 and 140 °C of reaction temperature. Subsequently, according to the Arrhenius Equation:

$$\ln \frac{k_2}{k_1} = -\frac{E_a}{R}\left(\frac{1}{T_2} - \frac{1}{T_1}\right)$$

where k_1 and k_2 are rate constants at temperature T_1 and T_2, and R is the molar gas constant (8.314 J mol^{-1} K^{-1}), the activation energy $E_a = 66.5$ kJ/mol can be calculated. This result is close to but lower than the previous investigation by Nie et al. [9]. In sharp contrast,

Fig. 7. Reaction activities and selectivities toward DFF and FFCA changed with O_2 pressures for HMF oxidation. (a) Low concentration of 1.0 mmol of HMF dissolved in 10 mL H_2O. (b) High concentration of 5.0 mmol of HMF dissolved in 10 mL H_2O (130 °C, 0.5–5 MPa O_2, 100 mg VO_x-ms, 1 h).
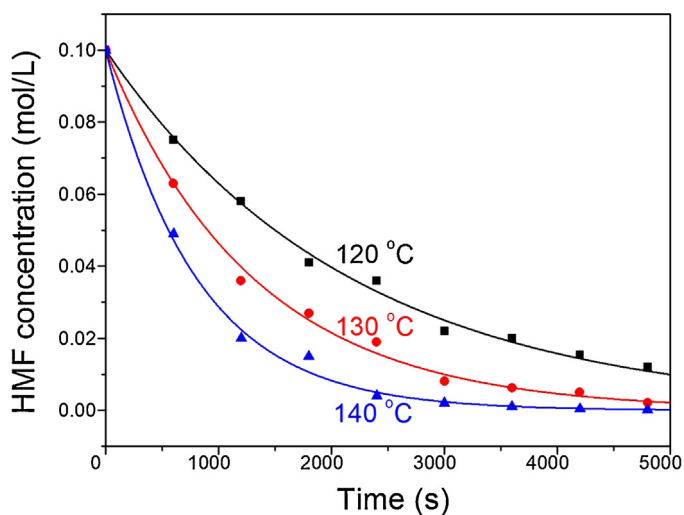
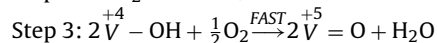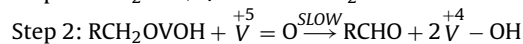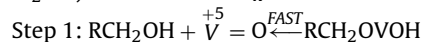**Fig. 8.** Three curves for HMF concentrations (recorded every 10 min) changed with the reaction time duration at 120 °C, 130 °C and 140 °C, respectively. This [HMF]-t plots can be fitted for reaction rate equations (3 MPa O_2, 1.0 mmol HMF, 10 mL H_2O, 100 mg VO_x-ms).

other reported reaction rate equations involve a half-order dependence on O_2 concentration for HMF oxidation over manganese oxide catalysts [4], where O_2 pressure is only 0.5 MPa. Since our reaction condition employed excessive 3 MPa of O_2, the influence of O_2 concentration on reaction rate can be neglected. The pseudo first order kinetics of HMF oxidation on Ag-OMS-2 catalyst reported by Yadav and Sharma [23] is very similar to our first order model, which will be further verified by isotopic and mechanism studies.

3.4. Reaction mechanism and kinetics of HMF oxidation

According to the discussion above, the activities of VO_x-ms catalyst rely upon high exposure degree of (0 1 0) facet, strong hydrogen adsorption capability and steric advantage of V=O sites on (0 1 0) facet. Such sites possess strong hydrogen adsorption capability for HMF O-H and αH-C bonds cleavage. It was reported that αH-C bond cleavage step was kinetic-relevant step for alcohol oxidation reaction [4,9,24]. In order to understand the kinetic roles of αH-C and O-H bonds cleavage in HMF oxidation on VO_x-ms, isotopic study was carried out using HMF molecules with deuterated hydroxyl group (R-CH_2OD) and with deuterated methylene group (R-CD_2OH). As shown in Table 3, where k_H/k_D is defined as reaction activity ratio of undeuterated and deuterated HMF oxidation at 130 °C 3 MPa O_2. The R-CH_2OD gave the k_H/k_D of 1.05, close to unity, implying the dissociative adsorption of HMF to form adsorbed intermediate reaches quasi-equilibrium and is kinetically unimportant in HMF oxidation over VO_x-ms catalyst. Whereas, R-CD_2OH gave the k_H/k_D of 2.21, larger than unity, suggesting the αH-C bond cleavage is kinetically relevant (or rate-determining step) in HMF oxidation on VO_x-ms. The dissociative chemisorption of O_2 into lattice O is irreversible, which was substantiated by oxygen isotope exchange between $^{18}O_2$ and $^{16}O_2$ consequently showing no trace of $^{18}O^{16}O$ isotopomer under the same reaction conditions. $H_2^{18}O$ was detected in product phase. However, $V^{18}O_x$ cannot be detected in collected and dried catalyst solid after reaction, suggesting no exchange of oxygen between gaseous O_2 and VO_x-ms occurred during reaction. Therefore, the elementary steps may involve hydrogen transfer processes in HMF oxidation using VO_x-ms

According to the kinetic and isotopic analysis, we propose simplified three element steps to explain mechanism for HMF (RCH_2OH) oxidation on VO_x-ms.

Step 1: $RCH_2OH + \overset{+5}{V} = O \overset{FAST}{\longleftarrow} RCH_2OVOH$

Step 2: $RCH_2OVOH + \overset{+5}{V} = O \overset{SLOW}{\longrightarrow} RCHO + 2\overset{+4}{V} - OH$

Step 3: $2\overset{+4}{V} - OH + \frac{1}{2}O_2 \overset{FAST}{\longrightarrow} 2\overset{+5}{V} = O + H_2O$

Dissociative chemisorption of HMF is proceeded preferably on the V=O sites on facet (0 1 0) due to the strong hydrogen adsorption capability and steric advantage of such sites (Step 1, fast). Subsequently, the intermediate RCH_2OVOH is irreversibly oxidized by lattice oxygen on V=O through αH-C bond cleavage to form DFF (RCHO) and the reduction product V-OH (Step 2, slow). Consequently, the V-OH is irreversibly oxidized by molecular oxygen to recover the lattice oxygen of V=O (Step 3, fast). Compared to the mechanism involving V^{5+}/V^{4+} redox cycles and V^{4+} re-oxidation by O_2 proposed by Nie et al. [9], the vanadium valence change in our study is reflected by hydrogen transfer in the V=O/V-OH redox cycles, and similarly, V-OH is further oxidized by O_2.

Introducing the pseudo-steady state assumption for chemisorbed intermediates and quasi-equilibrium assumption for Step 1, taking Step 2 as the rate-determining step, the rate equation for HMF oxidation on VO_x-ms can be derived as below.

For quasi-equilibrium assumption:

$$k_1[RCH_2OH][V = O] = k_{-1}[RCH_2OVOH] \tag{1}$$

Table 3
Kinetic isotopic effects on catalytic performance for HMF oxidation on VO_x-ms.[a]

Reactant	Conversion (%)	Activity (mmol/(g_{cat}h))	Selectivity (%)			k_H/k_D
			DFF	FFCA	FDCA	
RCH_2OH	93.7	9.37	95.4	3.2	1.4	–
RCH_2OD	89.2	8.92	93.4	4.5	2.1	1.05
RCD_2OH	42.4	4.24	87.9	9.8	2.3	2.21

[a] 130 °C, 3 MPa O_2, 1.0 mmol HMF, 10 mL H_2O, 100 mg VO_x-ms, 1 h.

$$r = k_2[V=O][RCH_2OVOH] = \frac{k_1 k_2}{k_{-1}}[V=O]^2[RCH_2OH] \quad (2)$$

For pseudo-steady state assumption (the adsorbed intermediate RCH_2OVOH concentration keeps steady):

$$\frac{d[RCH_2OVOH]}{dt} = k_1[RCH_2OH][V=O] - k_{-1}[RCH_2OVOH]$$
$$- k_2[RCH_2OVOH][V=O] \quad (3)$$

$$[RCH_2OVOH] = \frac{k_1[RCH_2OH][V=O]}{k_{-1} + k_2[V=O]} \quad (4)$$

$$r = \frac{k_1 k_2[RCH_2OH][V=O]^2}{k_{-1} + k_2[V=O]} \approx \frac{k_1 k_2}{k_{-1}}[V=O]^2[RCH_2OH]$$
$$(k-1 \gg k2[V=O]) \quad (5)$$

The results derived from two assumptions are in line with each other. Since [V=O] is sufficient and remains constant in VO_x-ms catalyst when reactant concentration is low (avert full coverage of surface V=O), such reaction rate equation presents a first order reaction and rate linearly spaced with HMF concentration, in fine agreement with the experimental results given by Fig. 8. Thus, the rate equation is simplified to be:

$$r = k[HMF], \quad k = \frac{k_1 k_2}{k_{-1}}[V=O]^2 \quad (6)$$

Since VO_x-ms can be regarded as micro-reactors with certain residence time distribution, catalytic conversion and yields are also dependent upon residence time distribution.

4. Conclusions

We have prepared a hierarchical structure of vanadium oxide nanobelt-arrayed microspheres through solvothermal method and calcination at 350 °C. This material affords high catalytic activity (conversion 93.7%) and selectivity (95.4%) for HMF oxidation to DFF, compared to other vanadium oxides catalysts such as bulk V_2O_5, VO_2 and V_2O_3. Such remarkable catalytic performance can be ascribed to major exposure of (0 1 0) facet, strong hydrogen adsorption capability and steric advantage of V=O sites on (0 1 0) facet proved by DFT calculations, high effective surface area, specific nanobelt-arrayed morphology for residence time control. The convenience of hydrogen bond between lattice oxygen and the O-H group of HMF also facilitates the high selectivity for contact and oxidation of -CH_2OH instead of the–CHO group on HMF, leading to high selectivity toward DFF. Isotopic studies derived the element steps for mechanism study with αH-C bond cleavage using lattice V=O sites as the rate-determining step. Reaction mechanism involves hydrogen transfer in the V=O/V-OH redox cycles and V-OH re-oxidation by O_2. In addition, a first-order reaction rate equation dependent upon HMF concentration has been derived based on pseudo-steady state and quasi-equilibrium assumptions. Activation energy of HMF oxidation catalyzed by VO_x-ms (66.5 kJ/mol) has also been calculated according to Arrhenius Equation. Such penetrated investigation of structural requirements, active sites distribution, mechanism and kinetic studies can offer a rationale for future design of more efficient catalysts for selective HMF oxidation to DFF or other valuable products.

References

[1] J.H. Lan, J.C. Lin, Z.Q. Chen, G.C. Yin, ACS Catal. 5 (2015) 2035–2041.
[2] G.Q. Lv, H.L. Wang, Y.X. Yang, T.S. Deng, C.M. Chen, Y.L. Zhu, X.L. Hou, ACS Catal. 5 (2015) 5636–5646.
[3] J.J. Roylance, T.W. Kim, K.S. Choi, ACS Catal. 6 (2016) 1840–1847.
[4] J. Nie, H. Liu, J. Catal. 316 (2014) 57–66.
[5] A. Takagaki, M. Takahashi, S. Nishimura, K. Ebitani, ACS Catal. 1 (2011) 1562–1565.
[6] C.A. Antonyraj, B. Kim, Y. Kim, S. Shin, K.-Y. Lee, I. Kim, J.K. Cho, Catal. Commun. 57 (2014) 64–68.
[7] X. Jia, J. Ma, M. Wang, Z. Du, F. Lu, F. Wang, J. Xu, Appl. Catal. A-Gen. 482 (2014) 231–236.
[8] L. Ngoc-Thuc, P. Lakshmanan, K. Cho, Y. Han, H. Kim, Appl. Catal. A-Gen. 464 (2013) 305–312.
[9] J.F. Nie, H.C. Liu, Pure Appl. Chem. 84 (2012) 765–777.
[10] X.K. Li, Y.G. Zhang, Green Chem. 18 (2016) 643–647.
[11] B. Delley, J. Chem. Phys. 113 (2000) 7756–7764.
[12] J. Goclon, R. Grybos, M. Witko, J. Hafner, Phys. Rev. B 79 (2009) 075439.
[13] M. Calatayud, B. Mguig, C. Minot, Surf. Sci. 526 (2003) 297–308.
[14] M. Calatayud, F. Tielens, F. De Proft, Chem. Phys. Lett. 456 (2008) 59–63.
[15] J. Goclon, R. Grybos, M. Witko, J. Hafner, J. Physics-Condensed Matter 21 (2009).
[16] E. Hryha, E. Rutqvist, L. Nyborg, Surf. Interface Anal. 44 (2012) 1022–1025.
[17] Y. Yan, K. Li, L. Thia, Y. Dai, J. Zhao, X. Chen, Y. Yang, J.-M. Lee, Environ. Sci.: Nano 3 (2016) 701–706.
[18] Y.B. Yan, K.X. Li, Y.H. Dai, X.P. Chen, J. Zhao, Y.H. Yang, J.M. Lee, Electrochim. Acta 208 (2016) 231–237.
[19] Y. Yan, K. Li, Y. Dai, X. Chen, J. Zhao, Y. Yan, J. Huang, Y. Yang, J.-M. Lee, Adv. Mater. Interfaces 3 (2016) 1500833.
[20] R. Ramirez, B. Casal, L. Utrera, E. Ruizhitzky, J. Phys. Chem. 94 (1990) 8960–8965.
[21] J.F. Nie, J.H. Xie, H.C. Liu, J. Catal. 301 (2013) 83–91.
[22] K. Yamaguchi, N. Mizuno, Chem.-A Eur. J. 9 (2003) 4353–4361.
[23] G.D. Yadav, R.V. Sharma, Appl. Catal. B-Environ. 147 (2014) 293–301.
[24] V.D. Makwana, Y.C. Son, A.R. Howell, S.L. Suib, J. Catal. 210 (2002) 46–52.